(This is a sample cover image for this issue. The actual cover is not yet available at this time.)

European Journal of Mechanics A/Solids 30 (2011) 807–819

Contents lists available at ScienceDirect

European Journal of Mechanics A/Solids

journal homepage: www.elsevier.com/locate/ejmsol

A study of the Yld2004 yield function and one extension in polynomial form: A new implementation algorithm, modeling range, and earing predictions for aluminum alloy sheets

Stefan C. Soare [a,*], Frédéric Barlat [b]

[a] Technical University of Cluj-Napoca, 28 Memorandumului, 400114 Cluj-Napoca, Romania
[b] Pohang University of Science and Technology, San 31, Hyoja-dong, Nam-gu, Pohang, Gyeongbuk 790-784, Republic of Korea

ARTICLE INFO

Article history:
Received 3 February 2011
Accepted 19 May 2011
Available online 30 May 2011

Keywords:
Anisotropy
Yield function
Sheet metal
Finite element method
Deep Drawing

ABSTRACT

As shown recently in (Soare and Barlat, 2010. Convex polynomial yield functions. J. Mech., Phys. Solids, 58, 1804–1818), the principal values based yield function Yld2004, proposed in (Barlat et al., 2005. Linear transformation based anisotropic yield function. Int. J. Plast., 21, 1009–1039), is polynomial for integer exponents. Based on this observation, a new algorithm is proposed for implementing symmetric yield functions formulated in terms of principal values. The algorithm is tested here by simulating with a commercial FE code the cylindrical deep drawing of two aluminum sheets. It is found that the classical description of the in-plane directional properties of the sheet (uniaxial *r*-values and yield stresses), even if modeled correctly by the yield function, is not sufficient for a unique characterization of the predicted earing profile. For certain combinations of the directional properties the *r*-value in biaxial stressing has to be considered for a correct calibration of the material model. This in turn requires a finer detail in yield surface modeling and, to achieve it, an ad-hoc extension of Yld2004 is constructed. In combination with the proposed implementation algorithm, the extension is shown to be a useful research tool, having some interesting modeling capabilities and satisfactory FE runtime.

1. Introduction

The yield surface concept lies at the core of the phenomenological description of the plastic deformation in metals. In associated plasticity, it models both the yielding and the plastic flow of the material. Because of this dual role of the yield surface, particular care for its modeling is required. Furthermore, given the complexity of the underlying mechanism of plastic flow (single and polycrystal plasticity), and the increasingly advanced alloying technologies, a certain complexity in yield surface modeling and an increase in the number of material parameters are to be expected. These trends in yield surface development are already visible in a number of recent contributions: Hosford (1972), Boehler (1987), Hill (1990), Karafillis and Boyce (1993), Barlat et al. (2005), to mention just a few representative approaches that have led to further developments.

In Soare and Barlat (2010) it was shown that some of the recent yield function models, e.g. Barlat et al. (2005), are polynomial functions. Based on this observation, a new algorithm for implementing symmetric principal values based yield functions is proposed in the present work. The algorithm is tested here for accuracy and efficiency by simulating the deep drawing of cylindrical cups.

In cylindrical deep drawing, a disk-shaped blank cut out from a sheet metal is placed concentrically over a die with cylindrical cavity and drawn into by a cylindrical punch (here with flat bottom); a holder pressures the blank during drawing to avoid wrinkling. The resulting cup has a non-uniform height, featuring symmetric local maxima (ears) and minima. Given the circular symmetry of the forming process, this phenomenon is explained by the anisotropic plastic properties of the sheet. Motivated in part by its practical implications (each year, billions of aluminum beverage cans are produced worldwide), the deep drawing problem has been studied intensively during the past decades, using both phenomenological and physical based approaches for modeling the response of sheet metal. In the present work only the effects of the initial anisotropy are investigated, and it is shown to explain much of the non-uniformity, if modeled correctly.

One additional feature of yield functions with relatively large sets of parameters, unnoticed previously, it seems, is that although

* Corresponding author.
E-mail address: stef_soare@yahoo.com (S.C. Soare).

0997-7538/$ – see front matter © 2011 Elsevier Masson SAS. All rights reserved.
doi:10.1016/j.euromechsol.2011.05.006

they are capable of accurate descriptions of the in-plane directional (uniaxial) properties of a sheet metal, they may predict sensibly different plastic properties for neighboring stress states. This phenomenon is evidenced in the present work in the case of deep drawing simulations. It will be shown that an incorrect description of the *r*-value of the material on the flange area (not at the rim) may affect significantly the profile predictions, and, conversely, that an adequate calibration of the yield surface model leads to more coherent predictions. Previous earing profile predictions, seemingly contradictory, e.g. Yoon et al. (2006), Kim et al. (2008), Rabahallah et al. (2009), may be explained by investigating the corresponding modeling of the biaxial *r*-values. Furthermore, the calibration of strain-rate potentials and of other texture-based models may also benefit from this observation, e.g., Arminjon et al. (1994), Van Houtte et al. (2006).

2. The Yld2004 function and its polynomial representation/implementation

The set of slip systems of a single crystal and the texture of a polycrystal are two essential constitutive features that govern the plastic deformation of sheet metal, Hosford (1993), Kocks et al. (2000). Based on polycrystal calculations, Hershey (1954) and later Hosford (1972) proposed the following extension of the von Mises isotropic quadratic yield function:

$$f(\sigma) = \left\{(1/2)\left[(\sigma_1-\sigma_2)^n+(\sigma_2-\sigma_3)^n+(\sigma_3-\sigma_1)^n\right]\right\}^{1/n} \tag{1}$$

with σ_i denoting the principal values of the Cauchy stress tensor σ. In Hosford's theory, the exponent n was associated with the crystal structure: $n = 6$ and $n = 8$ were recommended for modeling isotropic approximations of BCC and FCC polycrystals, respectively. Barlat et al. (2005) extended Hosford's approach to an anisotropic formulation by defining

$$\begin{aligned} 4f^n(\sigma) = {} & \left(\Sigma_1^{(1)}-\Sigma_1^{(2)}\right)^n+\left(\Sigma_1^{(1)}-\Sigma_2^{(2)}\right)^n+\left(\Sigma_1^{(1)}-\Sigma_3^{(2)}\right)^n \\ & +\left(\Sigma_2^{(1)}-\Sigma_1^{(2)}\right)^n+\left(\Sigma_2^{(1)}-\Sigma_2^{(2)}\right)^n+\left(\Sigma_2^{(1)}-\Sigma_3^{(2)}\right)^n \\ & +\left(\Sigma_3^{(1)}-\Sigma_1^{(2)}\right)^n+\left(\Sigma_3^{(1)}-\Sigma_2^{(2)}\right)^n+\left(\Sigma_3^{(1)}-\Sigma_3^{(2)}\right)^n \end{aligned} \tag{2}$$

with $\Sigma_j^{(i)}$, $i = 1, 2$, denoting the principal values of two (symmetric) image stresses $\Sigma^{(i)}$ defined by

$$\begin{aligned} \Sigma_x^{(i)} &= \alpha_1^{(i)}\sigma_x+\alpha_2^{(i)}\sigma_y-\left(\alpha_1^{(i)}+\alpha_2^{(i)}\right)\sigma_z,\ \Sigma_y^{(i)} = \alpha_3^{(i)}\sigma_x+\alpha_4^{(i)}\sigma_y-\left(\alpha_3^{(i)}+\alpha_4^{(i)}\right)\sigma_z \\ \Sigma_z^{(i)} &= \alpha_5^{(i)}\sigma_x+\alpha_6^{(i)}\sigma_y-\left(\alpha_5^{(i)}+\alpha_6^{(i)}\right)\sigma_z,\ \Sigma_{xy}^{(i)} = \alpha_7^{(i)}\sigma_{xy},\ \Sigma_{xz}^{(i)} = \alpha_8^{(i)}\sigma_{xz}, \Sigma_{yz}^{(i)} = \alpha_9^{(i)}\sigma_{yz} \end{aligned} \tag{3}$$

The components σ_x, Σ_x, etc, are taken with respect to a material Cartesian coordinate system (detailed in the next section). In what follows, the function f defined in (2) will be referred to as Yld2004. The parameters of Yld2004 are the coefficients $\alpha_j^{(i)}$ of the two transformation tensors. In particular, Hosford's criterion, the isotropic case, is recovered by imposing the conditions $\Sigma^{(1)} = \sigma' = \Sigma^{(2)}$, with $\sigma' = \sigma - tr(\sigma)/3$ denoting the stress deviator:

$$\begin{aligned} &\alpha_1^{(1)} = \alpha_1^{(2)} = 2/3,\ \alpha_2^{(1)} = \alpha_2^{(2)} = -1/3,\ \alpha_3^{(1)} = \alpha_3^{(2)} = -1/3,\ \alpha_4^{(1)} = \alpha_4^{(2)} = 2/3, \\ &\alpha_5^{(1)} = \alpha_5^{(2)} = -1/3,\ \alpha_6^{(1)} = \alpha_6^{(2)} = -1/3,\ \alpha_7^{(1)} = \alpha_7^{(2)} = \alpha_8^{(1)} = \alpha_8^{(2)} = \alpha_9^{(1)} = \alpha_9^{(2)} = 1 \end{aligned} \tag{4}$$

The original formulation of Yld2004 in eq. (2) requires the calculation of the principal values of the two image stresses. For general 3D stress states this is a rather complicated procedure since it should use several charts for mapping the three solutions of the characteristic equation. For plane stress states (2D) the characteristic equation is solvable by square roots, but for certain (highly symmetric) combinations of material parameters there are nonzero stress states that render the gradient of the yield function singular, a phenomenon due to the analytical formula used for calculations (square roots) and not to the intrinsic formulation.

A simpler implementation strategy for Yld2004 is obtained if its polynomial form is used instead. With Newton's binomial formula, eq. (2) is rewritten as follows, Soare and Barlat (2010):

$$f^n(\sigma) = \sum_{p=0}^{n} W_n Q_{n-p}\left(\Sigma^{(1)}\right) Q_p\left(\Sigma^{(2)}\right) \tag{5}$$

where $W_n := (-1)^p n!/[p!(n-p)!]$, and, for a generic image stress Σ,

$$Q_p(\Sigma) := (\Sigma_1)^p+(\Sigma_2)^p+(\Sigma_3)^p \tag{6}$$

Using the characteristic equation associated to an image stress Σ, the sums of powers Q_p satisfy in the 3D case

$$Q_p = I_1 Q_{p-1} + I_2 Q_{p-2} + I_3 Q_{p-3},\ p \geq 3 \tag{7}$$

with

$$I_1 := tr(\Sigma),\ I_2 := \left(\Sigma\cdot\Sigma - I_1^2\right)/2,\ I_3 := \det(\Sigma) \tag{8}$$

$$Q_0 = 3, Q_1 = I_1, Q_2 = (\Sigma_1)^2+(\Sigma_2)^2+(\Sigma_3)^2 = \Sigma\cdot\Sigma = I_1^2+2I_2 \tag{9}$$

In the 2D case, when $\sigma_z = \sigma_{xz} = \sigma_{yz} = 0$, we can safely distinguish $\Sigma_3 = \Sigma_z = \alpha_5\sigma_x+\alpha_6\sigma_y$, and then $Q_p = P_p+(\Sigma_3)^p$, where $P_p = (\Sigma_1)^p+(\Sigma_2)^p$, with the sums of powers P_p satisfying the simpler recurrence formula

$$P_p = I_1 P_{p-1} - I_2 P_{p-2}, p \geq 2 \tag{10}$$

where, this time, the invariants correspond to the 2×2 leading submatrix of Σ, call it S:

$$\begin{aligned} &I_1 := tr(S) = \Sigma_x+\Sigma_y,\ I_2 := \det(S) = \Sigma_x\Sigma_y-\left(\Sigma_{xy}\right)^2, \text{ and} \\ &P_0 = 2,\ P_1 = I_1 \end{aligned} \tag{11}$$

A finite element implementation requires the computation of the function value $f(\sigma)$, gradient $D\,f(\sigma)$, and hessian $H\,f(\sigma)$ (for implicit codes). All can be computed explicitly and fast, even for high homogeneity degrees, by using the above recurrence formulas. The algorithm is detailed in Appendix A. This

implementation was used in all the FE simulations featured in the present work.

3. Constitutive framework and integration algorithm

To study the effects of the initial anisotropy, and its mathematical representation, only, on earing predictions, the simplest constitutive model of plastic deformation has been adopted in this work. In essence, using a local description with respect to a material frame allows for a straightforward extension of the classical model for small strains to motions involving finite strains and finite rotations. Although restricted to a particular range of strain paths (along which an anisotropic evolution of the plastic properties can be neglected in a first approximation), this extension is sufficient for the current problem (one step deep drawing). In depth treatments of the relevant theory of plasticity algorithms and the nonlinear finite element method can be found in, e.g. Simo and Hughes (1998) and Belytschko et al. (2000).

The motion $x = x(X,t)$ of a body $B \subset \mathbb{R}^3$ is described with respect to a global orthonormal frame $\{e_i\}$. x denotes the spatial position of the material particle labeled $X \in B$ and identified as $X = x(X,t_0)$, with $t_0 = 0$ denoting the initial moment. $\{x_i\}$denotes the set of coordinates of position x. The polar decomposition of the deformation gradient $F = \partial x/\partial X$ reads: $F(X,\ t) = R(X,\ t)U(X,\ t) = V(x,\ t)R(X,\ t)$, with R denoting the orthogonal part of the local motion, and U, V the (right, left) stretch tensors. From the velocity field $v = \dot{x}$ one derives its spatial gradient $L(x,\ t) = \partial v/\partial x$, and, further, the basic decomposition of L into symmetric (rate of deformation) and antisymmetric (spin) parts: $L = D + W$, $D = (L + L^T)/2$, $W = (L - L^T)/2$.

A local orthonormal frame $\{\bar{e}_i = \bar{e}_i(X,\ t)\}$ is associated with each material point X of the anisotropic body B. The plastic properties of a small neighborhood of X will be characterized with respect to $\{\bar{e}_i\}$ and hence the local frame will also be referred to as the material frame. For a heterogeneous material the local frame features in general spatial variations. In what follows we assume a homogeneous body B and hence the initial orientation of the local frame is the same for all points $X \in B$. For example, in the case of an orthotropic sheet metal the local frame may be aligned along the three orthogonal symmetry axes of the sheet: the rolling direction (RD), transverse and normal directions, TD and ND. These are the axes with respect to which all the characterizing experiments (for determining the directional plastic properties of the sheet) are performed.

The constitutive response of the sheet at a (material) location X is described by a local observer at X and with respect to the material frame $\{\bar{e}_i\}$. The orientation of the local frame evolves according to:

$$\dot{\bar{e}}_i = Q(X,\ t)\bar{e}_i,\ \ \bar{e}_i(t_0) = R_0 e_i \tag{12}$$

with R_0 the orthogonal tensor specifying the initial orientation with respect to the global frame, and with Q an antisymmetric tensor, the spin rate determined by the motion. In the present work it is assumed that the initial characteristics of the anisotropy of the plastic properties are not affected by the deformation process. In particular, the local frame does not rotate with respect to its material neighborhood (no material rotation). Thus only spatial rotation is considered. Then the natural choice for the spin rate is $Q = \dot{R}R^T$, Tugcu and Neale (1999).

In what follows a line over the components of a second order tensor indicates that the coordinates are taken with respect to the local frame. Yielding of the material at particle X takes place when

$$f(\bar{\sigma}_{ij}) = H(\bar{\epsilon}^p) \tag{13}$$

with f denoting the yield function, H the (isotropic) hardening curve and $\bar{\epsilon}^p$ a measure of the accumulated plastic strain. By assuming small elastic strains, the total rate of deformation as perceived in the local frame $\{X,\ \bar{e}_i\}$ is additively decomposed into elastic and plastic parts

$$\bar{D}_{ij} = \bar{D}^e_{ij} + \bar{D}^p_{ij} \tag{14}$$

with the plastic part, during continuous yielding, characterized by the normality rule

$$\bar{D}^p_{ij} = \dot{\lambda}\frac{\partial f}{\partial \bar{\sigma}_{ij}}(\bar{\sigma}_{ij}) \tag{15}$$

The small elastic strains assumption is consistent with the relatively small (compared to their elastic counterparts) stresses sustained by metals during plastic deformation (even after hardening). Since $\dot{\lambda} > 0$ if and only if the body deforms plastically at X, $\dot{\lambda}$ can be taken as a measure of accumulation of plastic strain and hence

$$\dot{\bar{\epsilon}}^p = \dot{\lambda} \Leftrightarrow \bar{\epsilon}^p(t) = \bar{\epsilon}^p(t_0) + \int_{t_0}^{t} \dot{\lambda} d\tau \tag{16}$$

Finally, the stress–strain relationship characterizing the material response is assumed to take the hypo-elastic form

$$\dot{\bar{\sigma}}_{ij} = \bar{C}_{ijkl}\left(\bar{D}_{ij} - \bar{D}^p_{ij}\right) \tag{17}$$

with $\bar{C}_{ijkl} = C_{ijkl}$, the constant elasticity tensor C being assumed isotropic.

Summarizing, eqs. (13)–(17) define the response of the sheet metal. The algorithm for the numerical integration of these equations is presented in Appendix B. As a final remark, we note here that the above formulation is invariant (to spatial rigid motions) since the left member of the hypo-elastic law (17) is the (rotated) Green-Naghdi (objective) stress rate of the Cauchy stress. The Jaumann rate is used instead in some FE codes for 3D elements, e.g, ABAQUS (2004). The two rates are approximately equal for deformation paths involving moderate shear strains (like in the present case) and hence the same hypo-elastic law can be used with both rates. However, when shearing is significant (e.g., deep drawing followed by ironing) the hypo-elastic law should be modified accordingly for the Jaumann rate, Atluri (1984).

4. A first illustration: earing prediction for AA2090-T3

The performance of the new polynomial implementation of Yld2004 was first tested in the FE simulation of the deep drawing of the AA2090-T3 aluminum alloy described in Barlat et al. (2005) and

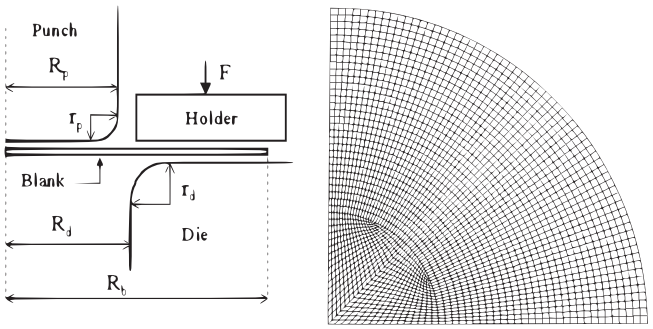

Fig. 1. Left: geometry of the deep drawing process. Right: the mesh on the blank used in all 2D deep drawing simulations (2494 elements, 2573 nodes).

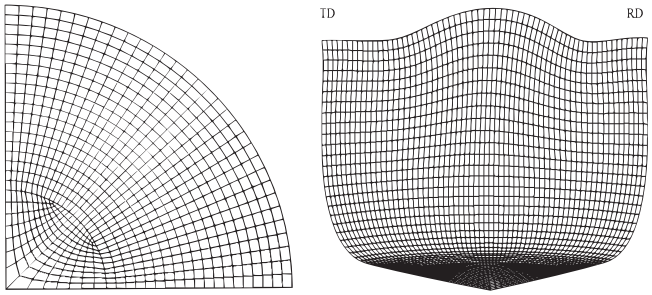

Fig. 2. Left: mesh on the blank used in the 3D simulation of the deep drawing of AA2090-T3 (2280 elements, 3212 nodes, three layers deep). Right: a final (quarter) cup (of the AA2090-T3 simulation with 2D elements).

for which deep drawing predictions were reported in Yoon et al. (2006). The material parameters of the Barlat et al. (2005) model of this alloy, referred in what follows as Model 0, are listed in Table 1 of Appendix C, in the notation of eq. (3).

In light of the assumed symmetry (orthotropic), only a quarter of the blank was modeled. Several simulations were conducted with 2D elements (Abaqus: S4R with 15 integration points across thickness) and 3D elements (Abaqus: C3D8R), both types of elements using reduced integration. The structures of the two meshes used for the blank, 2D and 3D, are shown in Figs. 1 and 2. The 3D mesh had three layers across thickness. Further technical details of the deep drawing simulations, together with the parameters of the deep drawing geometry described in Fig. 1, can be found in Appendix C.

The results (cup profiles) of the 2D and 3D simulations using the present implementation of Yld2004 are featured in Fig. 3. On a desktop computer (2 GHz processor) the CPU time for the 3D simulation was 8020.6 s (approx. 2 h:30 min wall clock time), while for the 2D simulation the CPU time was 12,164 s (approx. 4 h:30 min wall clock time). Also, comparison 2D simulations with the same coarser structure of the 3D mesh (and with similar final results) were conducted and required approx. 50 min (wall clock) to complete. Given the detail of the meshes, these run-times indicate a good performance of the polynomial implementation (the case $n = 8$); in the case of the coarser meshes, the runtime is comparable to the one reported in Yoon et al. (2006) for Yld2004 implemented in principal values form.

The agreement between the profiles resulted from the present simulation and the simulation of Yoon et al. (2006) is good, overall. The analysis of Kim et al. (2008) overestimates significantly the height of the 45°′ s ears. There is, however, a qualitative aspect predicted by both the present analyzes and Kim et al. (2008): the

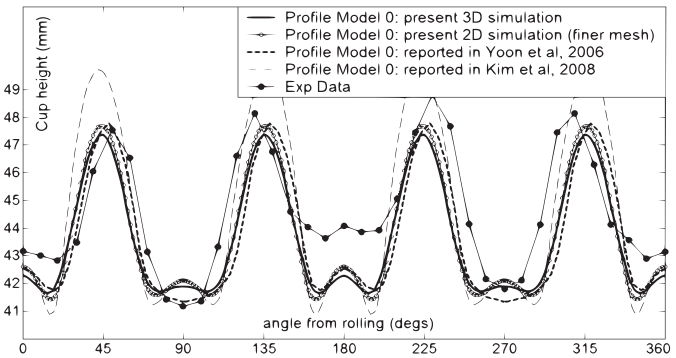

Fig. 3. Cup profiles of the Model 0 of AA2090-T3 reported in Barlat et al. (2005), predicted by the present 3D and 2D simulations. Also shown are the Model 0 predicted profiles reported in Yoon et al. (2006), Kim et al. (2008), and experimental data.

cup profiles feature eight ears, and not six, as reported in Yoon et al. (2006). Kim et al. (2008) made no attempt at explaining this phenomenon.

5. Earing analysis and an explanation of the previous results

The standard characterization of the plastic properties of the sheet is based on the classical directional r-values and yield stresses: elongated samples cut out from the sheet at several angles from the rolling direction are tested in uniaxial tension for their yielding stress and their capability to deform (r-value). Assuming a perfect symmetry in tension-compression of the plastic properties, this material characterization is complete for the rim of the blank, at least in the early moments of drawing: the rim is subjected to a compressive hoop stress only. Furthermore, one may note that the r-value measured in a direction θ from the RD, $r(\theta)$, characterizes the hoop strain at the rim in the direction $\pi/2 - \theta$. This observation led Yoon et al. (2006) to propose a very simple formula for predicting the shape of the cup profile based on the directional r-value only, formula that can be synthesized as follows: on the $[0^\circ, 90^\circ]$ interval the shape of the profile is the mirror symmetry of the directional r-value (more precisely, the profile has the same maxima and minima as the r-value). The predicted profile of the AA2090-T3 cup reported in the cited paper clearly agrees with this rule, while the present simulations contradict it by featuring two small additional ears along TD. By the above theory of earing, this could have happened if the r-value had a local maximum at 0° from RD.

At this point it is worth mentioning that even in the case when six ears are predicted for the cup profile, the two smaller ears along the TD may still develop at some point of the drawing phase and yet disappear by the end of the simulation. This phenomenon can be remarked on the profile history of the Poly6 model of AA2090-T3 reported in Soare et al. (2008). It can be explained by the reversal of the hoop stress from compressive to tensile during the last moments of drawing (when the material travels along the die shoulder). Too slow such a transition (favored in the present case by the smooth die shoulder) may lead to plastic straining in the opposite sense (hoop tension), removing any small ears that have developed previously, while the material was on the flange. Furthermore, it becomes clear that a constitutive assumption like kinematic hardening can have a significant effect upon the local minima of a cup profile, as tested in Yoon et al. (1998), and the small local maxima (the small ears). However, without a thorough understanding of the effects of initial anisotropy alone, it is difficult to discern the actual extent of the influence of kinematic hardening on the cup profile predictions.

The discrepancy between the results of the present simulations and the one of Yoon et al. (2006) may be explained by a particular type of contact used in the cited work (stick-after-contact for the die cavity and/or a small additional force to avoid frequent changes in contact status: these conditions increase further the tensile hoop stress during the last moments of drawing since the radius of the die is slightly larger than that of the punch and blank thickness combined). It will be shown, next, that Model 0 of AA2090-T3 agrees with an extended version of the above r-value based theory of earing and favors the prediction of a cup with eight ears, and not six, given the present simulation conditions (Appendix C) and constitutive model.

A closer look at the final deformation field featured by the drawn cup in Fig. 2 (the distortion of the mesh) reveals that, roughly, the upper half of the wall of the cup has suffered a non-uniform radial deformation. This part of the cup wall comprises all the material initially positioned between the punch wall and the rim of the blank (the flange area). During the drawing phase this material is subjected to a biaxial stress state: hoop compression and

radial traction (if neglecting the shear stress, friction and blank holding force). Assuming a plane stress state on the flange area, and that the hoop stress σ_θ is proportional with the drawing (radial) stress σ_r, the Cauchy stress components with respect to the local (material) frame of the blank are

$$\overline{\sigma}_x = \sigma_\theta\left(\cos^2\theta + q\sin^2\theta\right), \overline{\sigma}_y = \sigma_\theta\left(\sin^2\theta + q\cos^2\theta\right),$$
$$\sigma_{xy} = \sigma_\theta(1-q)\sin\theta\cos\theta \tag{18}$$

with r and θ denoting polar coordinates on the flange area. By assumption, $q := \sigma_r/\sigma_\theta = \text{constant}$ along any ring of material ($r = \text{constant}$). Practical considerations led Van Houtte et al. (1993) to approximate this stress ratio as uniform in the radial direction but the present assumption is more realistic since the material near the die shoulder is subjected to higher radial and smaller compressive stresses, the situation being reversed for the material near the rim of the blank. Since, in the present model, reversing the stress state does not affect the plastic properties, one may consider in eq. (18) that $\sigma_\theta > 0$ and $\sigma_r \leq 0$, and, in any case, that $q \leq 0$.

With the classical definition of the r-value (a comma denotes differentiation),

$$r_\theta = \frac{D_\theta}{D_z} = \frac{2f_{,\overline{\sigma}xy}(\overline{\sigma}_x,\overline{\sigma}_y,\overline{\sigma}_{xy})\cos\theta\sin\theta - f_{,\overline{\sigma}x}(\overline{\sigma}_x,\overline{\sigma}_y,\overline{\sigma}_{xy})\sin^2\theta - f_{,\overline{\sigma}y}(\overline{\sigma}_x,\overline{\sigma}_y,\overline{\sigma}_{xy})\cos^2\theta}{f_{,\overline{\sigma}x}(\overline{\sigma}_x,\overline{\sigma}_y,\overline{\sigma}_{xy}) + f_{,\overline{\sigma}y}(\overline{\sigma}_x,\overline{\sigma}_y,\overline{\sigma}_{xy})} \tag{19}$$

the classical r-value (uniaxial traction) is recovered for $q = 0$. We shall refer to the above r-value (with stress components given by eq. (18)) either as the extended r-value, or as the r-value in biaxial stressing.

Model 0 of AA2090-T3 is reconsidered next from this point of view: Fig. 4 features its extended directional properties and, for later shape comparisons, its yield surface. Most relevant for this discussion is the extended r-value, plotted here for several stress ratios: $q = 0$, for the material on the rim, and, as the die shoulder is approached, $q = -0.2$ (ratio determined from the FE analysis, and also consistent with the present drawing ratio, $d = R_b/R_p \approx 1.63$, Van Houtte et al. (1993)). While the classical r-value ($q = 0$) predicted by Model 0 features a local minimum at 0° from RD, the extended r-value has a local maximum at this location, for all the stress ratios $q \leq -0.05$. Thus, the material on the flange area is characterized by Model 0 with (qualitatively) different flow properties than those of the rim. Due to this characterization, the material on the flange along the TD direction strains faster than its radial neighbors, and hence favors the development of two additional small ears along TD: the earing profile predicted by the present simulations, Fig. 3, does indeed have the topology of the mirror image of the extended r-value, Fig. 4.

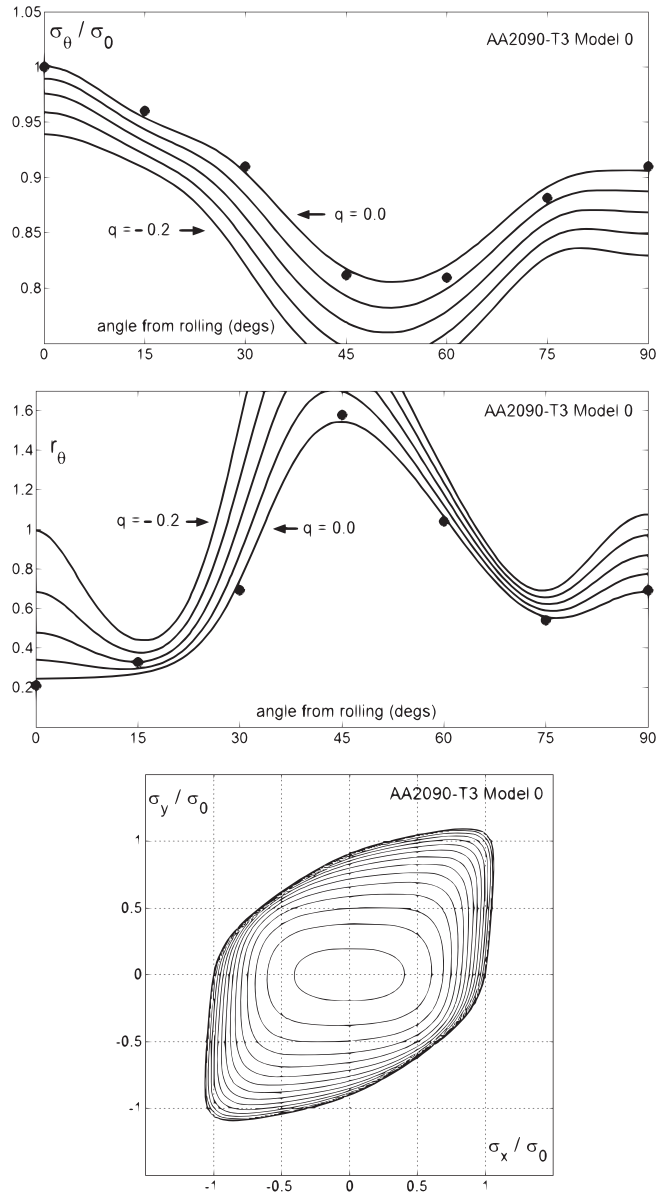

Fig. 4. Model 0 of AA2090-T3, Barlat et al. (2005): directional properties of the material on the flange, and $\sigma_{xy} = \text{const.}$ level curves (yield surface).

6. An extension of Yld2004 and reconsideration of the previous example

Since the actual AA2090-T3 cup features six ears, a better model of AA2090-T3 is required for predicting correctly (within the orthotropic approximation) its earing profile. This model should incorporate information about the plastic behavior under the biaxial stress in eq. (18). In fact, for this material, the only new information that needs to be added to the input data is about the plastic behavior along RD, since the rest of directions have well defined contributions to the overall topology of the r-value (local maxima and minima). Several trials for improving the Yld2004 Model 0 ($n = 8$) in this manner led to an overall increase in the distance between predictions and data: AA2090-T3 data is not sufficiently close to the modeling range of Yld2004 to allow for further improvements. In this respect, it is worth reminding that a general sixth order homogeneous polynomial, with 16 independent parameters, can give an almost perfect description, Soare et al. (2008), of the entire data set (7 + 7directional data, and the balanced-biaxial yield stress and r-value) reported for this alloy, Barlat et al. (2005). For $n = 8$, Yld2004 is generated by an eight order homogeneous polynomial. With Yld2004 having only 14 parameters, its modeling power will be increased here by adding

new parameters (up to 25 can be independent for its plane stress restriction, the number of parameters of the most general plane stress eight order homogeneous orthotropic polynomial).

An extension of Yld2004 that uses three image stresses has been recently proposed by Aretz et al. (2010). This extension also is based on Hosford's function, eq. (1). A better approach (from a computational point of view) is to combine the original Yld2004 with the Karafillis and Boyce (1993) generator as follows:

$$4f^n = P + Q_n\left(\Sigma^{(3)}\right) \tag{20}$$

with P denoting the right-hand member of eq. (2), and $\Sigma^{(3)}$ a third image stress. In what follows the above function will be referred to as Yld2004B. It has 21 parameters for modeling the in-plane plastic properties of the sheet. They can be identified by optimizing the distance between its predictions and data set

$$\begin{aligned} g\left(\alpha_p^{(k)}\right) &= \frac{1}{2}\sum_{j=1}^{j}\left[w_j^s\left(\sigma_{\theta_j} - Y_{\theta_j}\right)^2 + w_j^r\left(r_{\theta_j} - R_{\theta_j}\right)^2\right] \\ &+\frac{1}{2}\left[w_b^s(\sigma_b - Y_b)^2 + w_b^r(r_b - R_b)^2\right] \\ &+\frac{1}{2}\sum_j \overline{w}_j^r\left[\overline{r}_{\theta_j} - \overline{R}_{\theta_j}(q)\right]^2 + \dots \end{aligned} \tag{21}$$

where g is the distance (merit) function, the w's are weights, σ_θ, r_θ, $\overline{r}_\theta$, σ_b, r_b denote predicted values (with $\overline{r}_\theta$ an extended r-value, and the b subscript indicating balanced-biaxial), Y_θ denotes the experimentally measured directional yield stress (normalized with the yield stress in the rolling direction), R_θ denotes the experimental directional r-value, and $\overline{R}_\theta(q)$ denoting a hypothetical, yet, extended r-value corresponding to a stress ratio q. The dots in the above formula signify that different stress ratios can be used for the extended r-value, for the same material direction. Other data points, like the extended directional yield stress can also be added. The well known simplex algorithm of Nelder and Mead (1965) was used to solve

$$\text{Min}\, g\left(\alpha_p^{(k)}\right) \tag{22}$$

When implemented with a sequential stepping strategy (the input data is incrementally moved along the segment joining the predicted values of the initial guess and the target data points), this simple algorithm was able to find a solution with surprising ease.

Two models of AA2090-T3 were created using Yld2004B. Model 1 was intended to reproduce Model 0 with Yld2004B (with improved modeling of the classical directional and balanced-biaxial properties), while Model 2 was designed to feature a local minimum of the extended r-value along RD for most of the material traveling along the flange. For both models the input directional and balanced-biaxial data set was the same. The two models were distinguished by the extended r-value input data along RD and TD as follows:

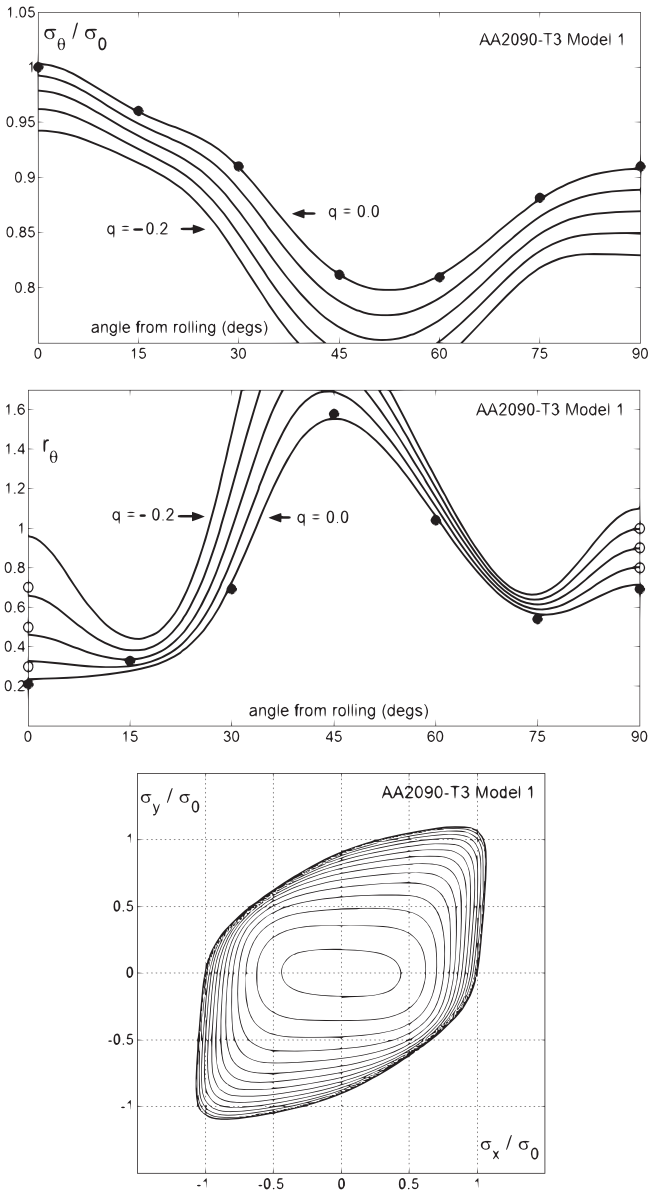

Fig. 5. Model 1 of AA2090-T3: directional properties of the material on the flange, and σ_{xy} = const. level curves (yield surface). Full circles denote the actual uniaxial data, whereas open circles indicate the extended r-values used as input. Designed to reproduce Model 0.

Models 1 and 2 of AA2090-T3 are presented in Figs. 5 and 6. The profiles of the cups resulting from the deep drawing simulations for Models 1 and 2 are featured in Fig. 7. The Model 1-profile reproduces the results obtained for Model 0, featuring eight ears.

$$\text{Model 1}\left\{\begin{array}{l}[\overline{R}_0(-0.05),\ \overline{R}_0(-0.1),\ \overline{R}_0(-0.15),\ \overline{R}_{90}(-0.05),\ \overline{R}_{90}(-0.1),\ \overline{R}_{90}(-0.15)] \\ = [0.8,\ 0.9,\ 1.0,\ 0.3,\ 0.5,\ 0.7]\end{array}\right.$$

$$\text{Model 2}\left\{\begin{array}{l}[\overline{R}_0(-0.05),\ \overline{R}_0(-0.1),\ \overline{R}_0(-0.15),\ \overline{R}_{90}(-0.05),\ \overline{R}_{90}(-0.1),\ \overline{R}_{90}(-0.15)] \\ = [0.77,\ 0.85,\ 0.9,\ 0.24,\ 0.26,\ 0.28]\end{array}\right.$$

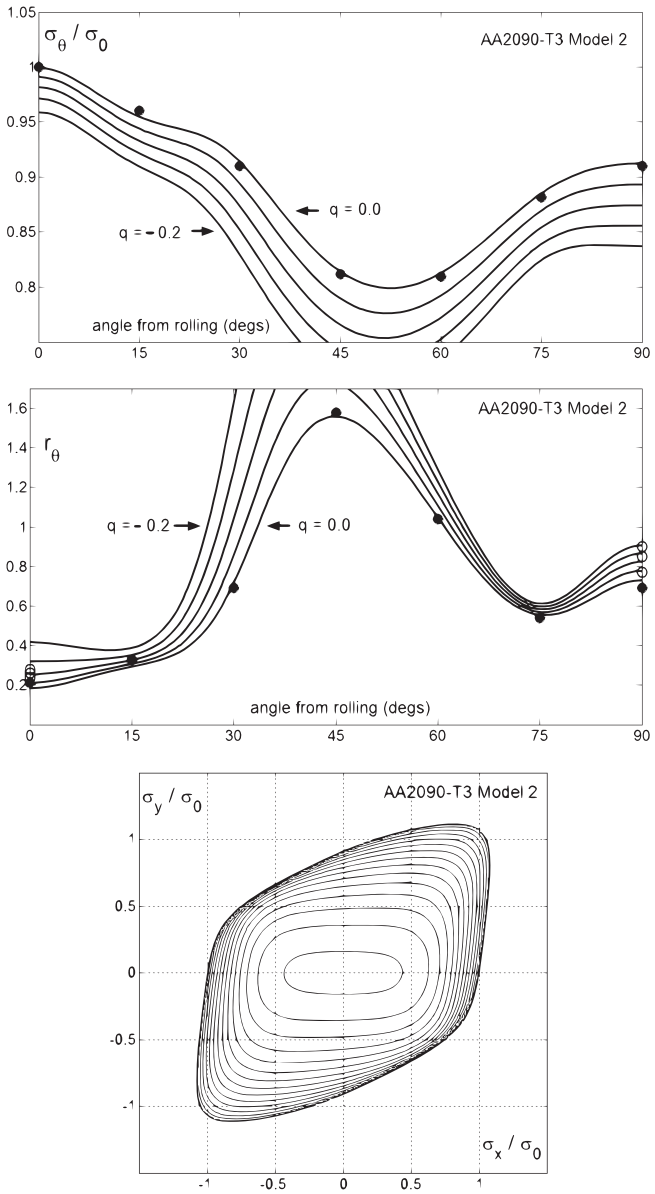

Fig. 6. Model 2 of AA2090-T3: directional properties of the material on the flange, and σ_{xy} = const. level curves (yield surface). Full circles denote the actual uniaxial data, whereas open circles indicate the extended r-values used as input. Designed to improve Model 0 (by flattening the local maximum of the extended r-value of Model 0 along RD).

Removing the local maximum of the extended r-values along RD, as done for Model 2, leads to the correct prediction: a profile with six ears. Furthermore, Model 2 has smaller extended r-values along TD than Model 1 and this explains the smaller ears along RD predicted by Model 1. Thus, we have created two models of the same material, with identical uniaxial directional and balanced-biaxial plastic properties, that predict qualitatively different cup profiles for cylindrically deep-drawn cups. This modeling exercise will be repeated in the next section for another aluminum alloy sheet.

7. A second illustration: modeling and earing prediction for AA3104-H19

In this section the alloy AA3104-H19 described in Aretz et al. (2010) is studied. Two directional 7-data points sets (yield stress

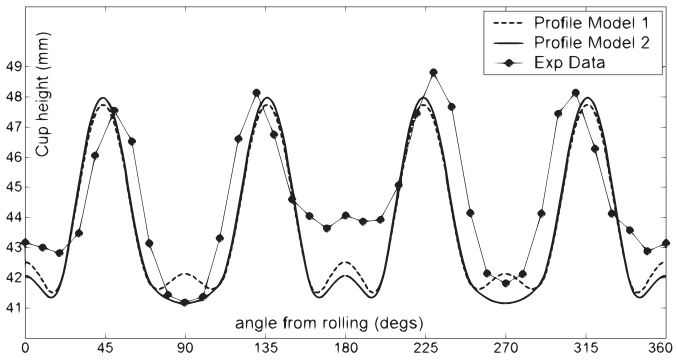

Fig. 7. Cup profiles predicted by the present Models 1 and 2 of AA2090-T3 (plane stress simulations).

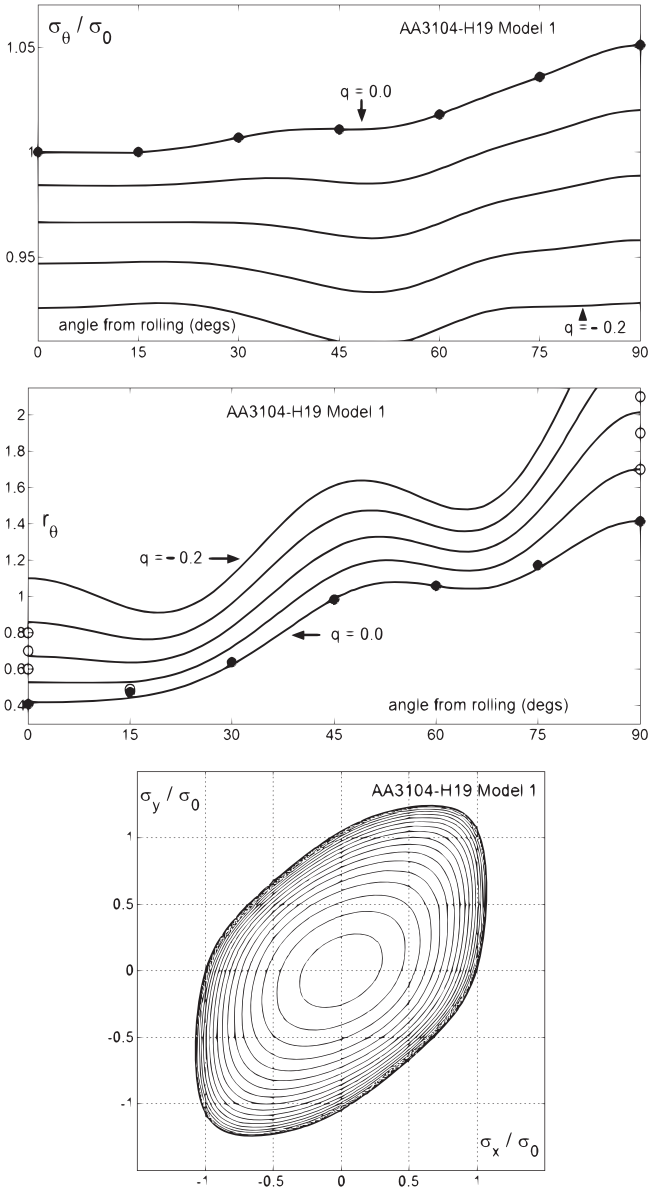

Fig. 8. Model 1 of AA3104-H19: directional properties of the material on the flange, and σ_{xy} = const. level curves (yield surface). Full circles denote the actual uniaxial data, whereas open circles indicate the extended r-values used as input.

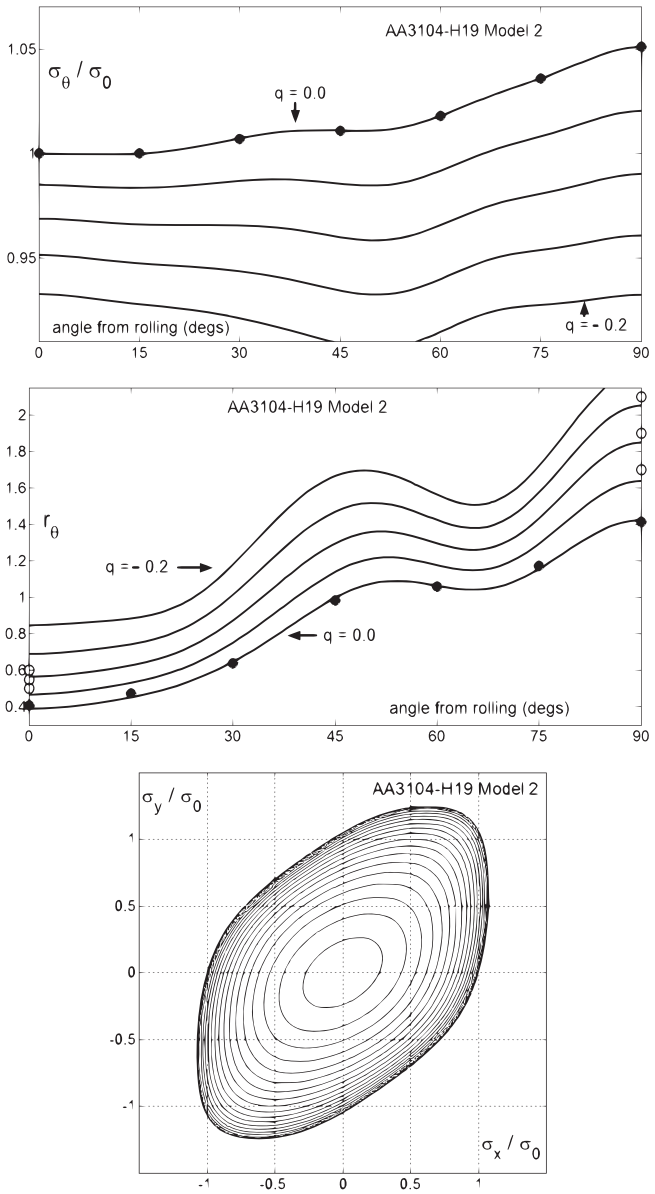

Fig. 9. Model 2 of AA3104-H19: directional properties of the material on the flange, and σ_{xy} = const. level curves (yield surface). Full circles denote the actual uniaxial data, whereas open circles indicate the extended *r*-values used as input.

and *r*-value) for uniaxial traction, and two plane strain yielding points along RD and TD are reported in the cited work. Additionally, the cited work used a plane strain yielding point measured from a test at 45° from RD. Instead of this point, the two balanced-biaxial predictions of the Aretz et al. (2010) yield surface model are used here. Two models of AA3104-H19 are created: both should represent all the above data points identically. The two models are differentiated by the input data used for the extended *r*-value:

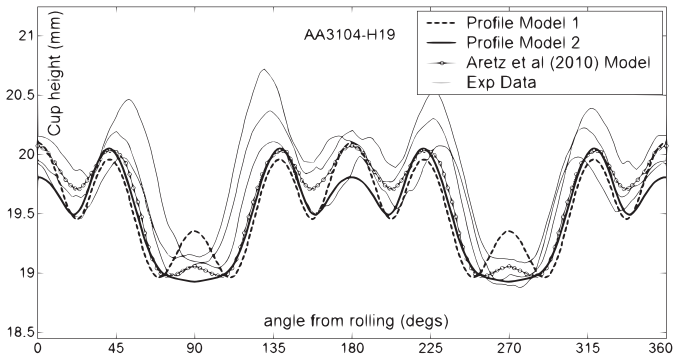

Fig. 10. Cup profiles predicted by Models 1 and 2 of AA3104-H19 (plane stress simulations). Comparison is made with the prediction of Aretz et al. (2010) and the several experimentally measured cup profiles reported there.

The two models of AA3104-H19 are presented in Figs. 8 and 9, and the corresponding cup profiles resulted from deep drawing simulations in Fig. 10. Model 1 is designed so that its extended *r*-value has a local maximum along RD, while Model 2 so that its extended *r*-value has a local minimum along RD. As a consequence, Model 2-profile features six ears, while Model 1-profile features eight ears (two extra ears along TD). Furthermore, for both Model 1 and Aretz et al. (2010)-profiles the height at 0° is greater than the height at 45°′ in contradiction with the reversed relationship observed in experiments. Finally, we note that the ears at 45°′ s from RD featured by all the predicted and measured profiles cannot be explained by the uniaxial directional properties alone. To explain the development of these ears, one has to consider the local maxima of the extended *r*-value in the interval $[45^{\circ}, 60^{\circ}]$, and the local minima of the extended directional stress in the same interval, as featured by both Model 1 and Model 2.

8. A third illustration: a hypothetical material

To test further the modeling capabilities of the Yld2004B extension and the influence of both the classical and extended *r*-values upon the shape of the cup profiles resulting from deep drawing simulations, a theoretical material, referred to as RMAT, is designed as follows. RMAT will have the same directional yielding stress as the AA2090-T3 sheet studied earlier. Its *r*-values will be modified as follows:

1) the classical *r*-value should be uniform;
2) the extended *r*-value (for nonzero stress ratios q) should feature two local maxima along RD and TD with one global minimum in between (a reversal of the global maximum featured by the actual AA2090-T3 material).

With input data constructed accordingly, the Yld2004B model of RMAT is presented in Fig. 11, while its parameters are listed in Appendix C. It can be noticed that the local minima of the

$$\text{Model 1}\left\{\begin{array}{l}[\overline{R}_0(-0.05),\ \overline{R}_0(-0.1),\ \overline{R}_0(-0.15),\ \overline{R}_{15}(-0.05),\ \overline{R}_{90}(-0.05),\ \overline{R}_{90}(-0.1),\ \overline{R}_{90}(-0.15)]\\ \quad = [0.6,\ 0.7,\ 0.8,\ 0.49,\ 1.7,\ 1.9,\ 2.1]\end{array}\right.$$

$$\text{Model 2}\left\{\begin{array}{l}[\overline{R}_0(-0.05),\ \overline{R}_0(-0.1),\ \overline{R}_0(-0.15),\ \overline{R}_{90}(-0.05),\ \overline{R}_{90}(-0.1),\ \overline{R}_{90}(-0.15)]\\ \quad = [0.5,\ 0.55,\ 0.6,\ 1.7,\ 1.9,\ 2.1]\end{array}\right.$$

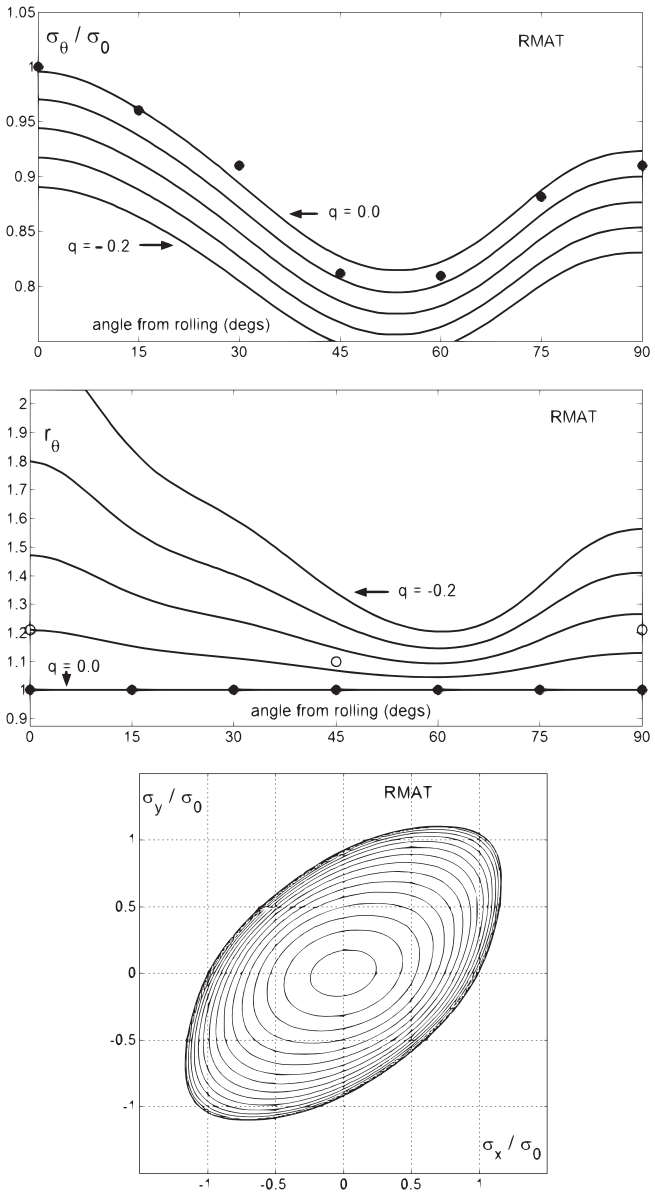

Fig. 11. A hypothetical material and its Yld2004B model: directional properties of the material on the flange, and σ_{xy} = const. level curves (yield surface). Full circles denote classical directional properties used as input, and open circles denote the extended *r*-values ($q = -0.05$) used as input.

directional stress and extended *r*-value are almost coincident (around 55°′ and 60°′ respectively). The cup profile resulting from a deep drawing simulation performed in precisely the same conditions as for the actual AA2090-T3 material is shown in Fig. 12. The simulated cup features only four ears in the 45°′ s directions. A theory of the cup profile based on the classical *r*-value would predict that the profile should be uniform; a theory based on the extended *r*-value would predict that the profile should feature four ears positioned along the rolling and transverse directions. The FE prediction proves that both theories are wrong for RMAT. In this case, the cause for ear development is the early yielding, and hence early plastic flow in the 45°′ s directions, as predicted by Hill (1950) theorem on earing. However, the directional yield stress of RMAT indicates a more ductile material along TD than RD and, based on this, an RMAT-cup with a height greater along RD than TD, contrary to the FE predicted cup. This inequality can be explained only by considering the extended *r*-value of RMAT : $\overline{R}_0(q) > \overline{R}_{90}(q),\ q \neq 0$.

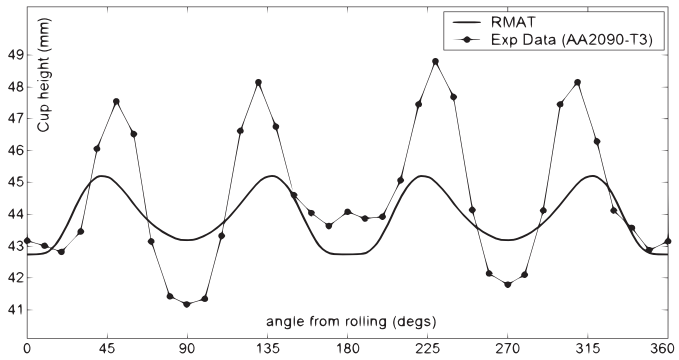

Fig. 12. Height profile of the predicted RMAT-cup drawn in the same conditions as the actual AA2090-T3 cup (plane stress simulation).

9. Further discussion and conclusions

An early theorem of Hill (1950) states that, during deep drawing, ears may develop in those directions that are critical points for the directional yield stress. Later work, e.g. Hosford and Caddell (1993) and references therein, or Duchene (2003), has shown a good correlation between ear development and the (uniaxial) *r*-value of the sheet. This line of investigation culminated with the mirror symmetry conjecture of Yoon et al. (2006) recalled earlier. That conjecture does not hold generally, as shown for a hypothetical material in Soare et al. (2008), and as seen here in the case of AA3104-H19. Although the extended *r*-value has been used successfully in the present work to improve upon the prediction of deep-drawn cup profiles, and although it may enlarge the range of validity of the above conjecture, cup profiles do not have, in general, the shape of the mirror image (on $[0^\circ,\ 90^\circ]$) of the extended *r*-value either, as shown here for the RMAT hypothetical material. Nevertheless, even in this hypothetical case the extended *r*-value does explain certain features of the cup profile that otherwise cannot be understood within a theory based on the classical directional properties only.

To conclude, the present work proposes a new algorithm for the implementation into finite element codes of yield functions formulated in terms of principal values of a set of image stresses and admitting polynomial reformulations. The recent Yld2004 proposed by Barlat et al. (2005) is one such example. When Yld2004 is tested with the new implementation in the simulation of cylindrical deep drawing, some deviations from previous reports are noticed in the case of AA2090-T3. These are explained here by an incomplete yield surface representation for this alloy. It is proposed, for deep drawing applications, if accuracy is of primary importance (e.g. earing prediction), that together with the classical uniaxial directional properties one should also consider extensions of these properties to biaxial stress states. This consideration leads to a more detailed description of the yield surface, but it also requires larger input data sets. With this purpose, the Yld2004 function (two image stresses) has been extended here, with minimum additional computational cost, to Yld2004B, a yield function employing three image stresses and with interesting modeling capabilities.

Acknowledgment

The authors thank J.-W. Yoon for sharing the minute details of his early AA2090-T3 deep drawing simulations. Thanks are addressed also to H. Aretz for providing the raw cup profile data for AA3104-H19. Finally, the first author acknowledges the support of the Romanian National Research Council (CNCS) in the frame of the Project PCCE 100/2010 “From micro to macro –

continuum scale modeling of advanced materials in virtual fabrication".

Appendix A. Implementation algorithm for symmetric yield functions of sums of powers

The following algorithm can be used with general yield functions of the form

$$f = f\left(Q_0^{(1)}, \ldots, Q_n^{(1)}, Q_0^{(2)}, \ldots, Q_n^{(2)}, \ldots\right) \tag{A.1}$$

with $Q_p^{(i)}$ corresponding to the i-th image stress and defined by eq. (7). In what follows the presentation is restricted to the Yld2004B analytical expression for the function f and to the 3D case, the simplification to the 2D case being straightforward.

The algorithm proceeds in two steps. In the first step the sequences $Q_p^{(i)}$ and their derivatives are calculated, while in the second step these sequences are assembled to calculate the yield function value and its derivatives. In the first step, the calculations detailed next for one generic image stress are repeated for each of the three image stresses of Yld2004B. The stress/strain components are stored in vector form following the ABAQUS convention

$$\sigma_1 := \sigma_{xx},\ \sigma_2 := \sigma_{yy},\ \sigma_3 := \sigma_{zz},\ \sigma_4 := \sigma_{xy},\ \sigma_5 = \sigma_{xz},\ \sigma_6 := \sigma_{yz}$$

and, as is customary in FE codes, the vectorial shear strains represent the double of the tensor strains. Other ordering conventions can be easily accommodated. The sub-steps for calculating the Q-powers associated with one image stress are then as follows.

Step 1.0

The yield function is first order positive homogeneous. This property is used to normalize the stress tensor and hence increase the number of significant digits used in computer arithmetics (all calculations in the present work, UMAT subroutine and element calculations, used double precision). Therefore we calculate the norm of the Cauchy stress σ, $S := (\sigma\cdot\sigma)^{1/2} + \epsilon$, with $\epsilon > 0$ a small number (constant), and define

$$s_i := \sigma_i/S,\ \ i = 1, \ldots, 6 \tag{A.2}$$

Step 1.1

Calculate the image stress, its invariants and their derivatives:

$$\Sigma_1 = \alpha_1 s_1 + \alpha_2 s_2 - (\alpha_1+\alpha_2)s_3,\ \Sigma_2 = \alpha_3 s_1 + \alpha_4 s_2 - (\alpha_3+\alpha_4)s_3,\ \Sigma_3 = \alpha_5 s_1 + \alpha_6 s_2 - (\alpha_5+\alpha_6)s_3,\ \Sigma_4 = \alpha_7 s_4,\ \Sigma_5 = \alpha_8 s_5,\ \Sigma_6 = \alpha_9 s_6 \tag{A.3}$$

$$I_1 = \Sigma_1 + \Sigma_2 + \Sigma_3,$$
$$I_2 = \frac{1}{2}\left[\Sigma_1^2 + \Sigma_2^2 + \Sigma_3^2 + 2\left(\Sigma_4^2 + \Sigma_5^2 + \Sigma_6^2\right) - I_1^2\right], \tag{A.4}$$

$$I_3 = \Sigma_1\Sigma_2\Sigma_3 + 2\Sigma_4\Sigma_5\Sigma_6 - \left(\Sigma_1\Sigma_6^2 + \Sigma_2\Sigma_5^2 + \Sigma_3\Sigma_4^2\right) \tag{A.5}$$

Note that in the above (polynomial) expressions of I_i, the tensorial shear image stress components are already doubled and hence further differentiation with respect to them requires no further precautions (doubling). Also, due to the pressure independence of the criterion, derivatives with respect to the normal stress σ_z need no intermediary calculations and hence they are calculated directly from the pressure independence condition in Step 2.2. Then, with a comma followed by a subscript indicating differentiation with respect to the corresponding Cauchy stress component, i.e., $I_{i,j} := \partial I_i/\partial\sigma_j$, and also omitting the zero derivatives, the relevant derivatives of the invariants are

$$I_{1,1} = \alpha_1 + \alpha_3 + \alpha_5,\ \ I_{1,2} = \alpha_2 + \alpha_4 + \alpha_6, \tag{A.6}$$

$$I_{2,1} = -[(\Sigma_2+\Sigma_3)\alpha_1 + (\Sigma_1+\Sigma_3)\alpha_3 + (\Sigma_1+\Sigma_2)\alpha_5], \tag{A.7}$$

$$I_{2,2} = -[(\Sigma_2+\Sigma_3)\alpha_2 + (\Sigma_1+\Sigma_3)\alpha_4 + (\Sigma_1+\Sigma_2)\alpha_6], \tag{A.8}$$

$$I_{2,4} = 2\Sigma_4\alpha_7,\ \ I_{2,5} = 2\Sigma_5\alpha_8,\ \ I_{2,6} = 2\Sigma_6\alpha_9, \tag{A.9}$$

$$I_{2,11} = -[(\alpha_3+\alpha_5)\alpha_1 + (\alpha_1+\alpha_5)\alpha_3 + (\alpha_1+\alpha_3)\alpha_5], \tag{A.10}$$

$$I_{2,21} = -[(\alpha_3+\alpha_5)\alpha_2 + (\alpha_1+\alpha_5)\alpha_4 + (\alpha_1+\alpha_3)\alpha_6], \tag{A.11}$$

$$I_{2,22} = -[(\alpha_4+\alpha_6)\alpha_2 + (\alpha_2+\alpha_6)\alpha_4 + (\alpha_2+\alpha_4)\alpha_6], \tag{A.12}$$

$$I_{2,44} = 2\alpha_7^2,\ \ I_{2,55} = 2\alpha_8^2,\ \ I_{2,66} = 2\alpha_9^2, \tag{A.13}$$

$$I_{3,1} = \left(\Sigma_2\Sigma_3 - \Sigma_6^2\right)\alpha_1 + \left(\Sigma_1\Sigma_3 - \Sigma_5^2\right)\alpha_3 + \left(\Sigma_1\Sigma_2 - \Sigma_4^2\right)\alpha_5, \tag{A.14}$$

$$I_{3,2} = \left(\Sigma_2\Sigma_3 - \Sigma_6^2\right)\alpha_2 + \left(\Sigma_1\Sigma_3 - \Sigma_5^2\right)\alpha_4 + \left(\Sigma_1\Sigma_2 - \Sigma_4^2\right)\alpha_6, \tag{A.15}$$

$$I_{3,4} = 2(\Sigma_5\Sigma_6 - \Sigma_3\Sigma_4)\alpha_7,\ I_{3,5} = 2(\Sigma_4\Sigma_6 - \Sigma_2\Sigma_5)\alpha_8,\ I_{3,6} = 2(\Sigma_4\Sigma_5 - \Sigma_1\Sigma_6)\alpha_9, \tag{A.16}$$

$$I_{3,11} = (\Sigma_3\alpha_3 + \Sigma_2\alpha_5)\alpha_1 + (\Sigma_3\alpha_1 + \Sigma_1\alpha_5)\alpha_3 + (\Sigma_2\alpha_1 + \Sigma_1\alpha_3)\alpha_5, \tag{A.17}$$

$$I_{3,21} = (\Sigma_3\alpha_3 + \Sigma_2\alpha_5)\alpha_2 + (\Sigma_3\alpha_1 + \Sigma_1\alpha_5)\alpha_4 + (\Sigma_2\alpha_1 + \Sigma_1\alpha_3)\alpha_6, \tag{A.18}$$

$$I_{3,41} = -2\Sigma_4\alpha_5\alpha_7,\ I_{3,51} = -2\Sigma_5\alpha_3\alpha_8,\ I_{3,61} = -2\Sigma_6\alpha_1\alpha_9, \tag{A.19}$$

$$I_{3,22} = (\Sigma_3\alpha_4 + \Sigma_2\alpha_6)\alpha_2 + (\Sigma_3\alpha_2 + \Sigma_1\alpha_6)\alpha_4 + (\Sigma_2\alpha_2 + \Sigma_1\alpha_4)\alpha_6, \tag{A.20}$$

$$I_{3,42} = -2\Sigma_4\alpha_6\alpha_7,\ I_{3,52} = -2\Sigma_5\alpha_4\alpha_8,\ I_{3,62} = -2\Sigma_6\alpha_2\alpha_9, \tag{A.21}$$

$$I_{3,44} = -2\Sigma_3\alpha_7^2,\ I_{3,54} = -2\Sigma_6\alpha_7\alpha_8,\ I_{3,64} = -2\Sigma_5\alpha_7\alpha_9, \tag{A.22}$$

$$I_{3,55} = -2\Sigma_2\alpha_8^2,\ \ I_{3,65} = 2\Sigma_4\alpha_8\alpha_9,\ \ I_{3,66} = -2\Sigma_1\alpha_9^2. \tag{A.23}$$

Step 1.2

Calculate the first three elements in the sequences $(Q_p)_p$, $(Q_{p,1})_p$, etc.

$$Q_0 = 3,\ \ Q_1 = tr(\Sigma) = I_1,\ \ Q_2 = I_1^2 + 2I_2$$
$$Q_{1,i} = I_{1,i},\ \ Q_{2,i} = 2(I_{1,i} + I_{2,i}),\ \ Q_{2,ij} = 2I_{2,ij}$$

Step 1.3

Use the recurrence formula (7) to calculate the rest of the needed elements in the sequences $(Q_p)_p$, $(Q_{p,1})_p$, etc. If n is the homogeneity degree, then.

For p from 3 to n DO

$$Q_p = I_1 Q_{p-1} + I_2 Q_{p-2} + I_3 Q_{p-3}$$

$$Q_{p,i} = I_{1,i} Q_{p-1} + I_1 Q_{p-1,i} + I_{2,i} Q_{p-2} + I_2 Q_{p-2,i} + I_{3,i} Q_{p-3} + I_3 Q_{p-3,i}$$

$$Q_{p,ij} = I_{1,i} Q_{p-1,j} + I_{1,j} Q_{p-1,i} + I_1 Q_{p-1,ij} + I_{2,ij} Q_{p-2} + I_{2,i} Q_{p-2,j} + I_{2,j} Q_{p-2,i} + I_2 Q_{p-2,ij} + I_{3,ij} Q_{p-3} + I_{3,i} Q_{p-3,j} + I_{3,j} Q_{p-3,i} + I_3 Q_{p-3,ij}$$

End DO

For the three image stresses of Yld2004B, the whole Q-sequences of the first two image stresses need to be stored for the final calculations in the next step, while the third image stress requires storage of the end entries only, i.e., $Q_n(\Sigma^{(3)})$, $Q_{n,i}(\Sigma^{(3)})$, etc.

Finally, calculate the function value, gradient and hessian. To this end, let P denote the n-th order homogeneous polynomial that defines the yield function, that is, $4f^n(\sigma) =: P(\sigma)$, and define $N := n/2$. Eq. (20) is rewritten as

$$P = Q_n\left(\Sigma^{(3)}\right) + W_{N+1} Q_{N+1}\left(\Sigma^{(1)}\right) Q_{N+1}\left(\Sigma^{(2)}\right) + \sum_{k=0}^{N} W_k \left[Q_k\left(\Sigma^{(1)}\right) Q_{n-k}\left(\Sigma^{(2)}\right) + Q_{n-k}\left(\Sigma^{(1)}\right) Q_k\left(\Sigma^{(2)}\right) \right]$$

where, for $n = 8$, the vector of binomial coefficients is $W = [1.0, -8.0, 28.0, -56.0, 70.0]$.

Step 2.1

Calculate P and its derivatives: initialize

$$P = Q_n\left(\Sigma^{(3)}\right) + W_{N+1} Q_{N+1}\left(\Sigma^{(1)}\right) Q_{N+1}\left(\Sigma^{(2)}\right)$$
$$P_{,i} = Q_{n,i}\left(\Sigma^{(3)}\right) + W_{N+1}\left[Q_{N+1,i}\left(\Sigma^{(1)}\right) Q_{N+1}\left(\Sigma^{(2)}\right) + Q_{N+1}\left(\Sigma^{(1)}\right) Q_{N+1,i}\left(\Sigma^{(2)}\right) \right]$$
$$P_{,ij} = Q_{n,ij}\left(\Sigma^{(3)}\right) + W_{N+1}\left[Q_{N+1,ij}\left(\Sigma^{(1)}\right) Q_{N+1}\left(\Sigma^{(2)}\right) + Q_{N+1,i}\left(\Sigma^{(1)}\right) Q_{N+1,j}\left(\Sigma^{(2)}\right) + \ldots \right]$$

and then add the rest of the terms of the polynomial expansion:

For k from 0 to N DO

$$P = P + W_k \left[Q_k\left(\Sigma^{(1)}\right) Q_{n-k}\left(\Sigma^{(2)}\right) + Q_{n-k}\left(\Sigma^{(1)}\right) Q_k\left(\Sigma^{(2)}\right) \right]$$
$$P_{,i} = P_{,i} + W_k \left[Q_{k,i}\left(\Sigma^{(1)}\right) Q_{n-k}\left(\Sigma^{(2)}\right) + Q_k\left(\Sigma^{(1)}\right) Q_{n-k,i}\left(\Sigma^{(2)}\right) + \ldots \right]$$
$$P_{,ij} = P_{,ij} + W_k \left[Q_{k,ij}\left(\Sigma^{(1)}\right) Q_{n-k}\left(\Sigma^{(2)}\right) + Q_{k,i}\left(\Sigma^{(1)}\right) Q_{n-k,j}\left(\Sigma^{(2)}\right) + \ldots \right]$$

End DO.

Step 2.2

Calculate yield function value and derivatives. Define

$$Y := (P/4)^{1/n}, \quad T := Y/(nP)$$

and then calculate the gradient,

$$f_{,i}(\sigma) = TP_{,i}(\sigma), \quad \text{for } i \neq 3, \quad \text{and } f_{,3}(\sigma) = -[f_1(\sigma) + f_{,2}(\sigma)]$$

the hessian,

$$f_{,ij} = \left[TP_{,ij} - (n-1) f_{,i} f_{,j} / Y \right] \Big/ S, \quad \text{for } i, j \neq 3, \quad \text{and}$$
$$f_{,31}(\sigma) = -[f_{,11}(\sigma) + f_{,21}(\sigma)], \quad \text{etc},$$

and, finally, the yield function value:

$$f(\sigma) = SY$$

Appendix B. Return mapping algorithm

The constitutive eqs. (15) and (17) form a nonlinear system of ordinary differential equations subject to the constraint (13). Explicit integration of this system of equations is impossible for general yield functions and hardening laws. This appendix presents the algorithm used in the present work for its numerical integration, an adaptation of the return mapping algorithm featured in Simo and Hughes (1998). The algorithm receives as input the previous material characteristics at the integration point (here, the equivalent plastic strain), the previous stress state and the current strain increment, and calculates the response of the material, that is, the new stress, its new material/plastic parameters, and an estimation of the elastic–plastic tangent modulus, denoted here by E^p.

In what follows all considerations refer to an arbitrary but fixed integration point and hence its specification shall be omitted. Let $[t_n, t_{n+1} := t_n + \Delta t]$ be the time interval over which the current strain increment $\Delta\epsilon$ takes place. t_n is the moment of the previous equilibrium state for which Σ_n and $\bar{\epsilon}_n^p$ are known. Here Σ denotes the matrix $[\bar{\sigma}_{ij}]$, of components in the local frame. The rotation over the current increment is calculated from the polar decomposition $\Delta F = \Delta R \Delta U = \Delta V \Delta R$ of the deformation gradient increment $\Delta F := F(t_{n+1}) F^{-1}(t_n)$. Assuming the principal stretching directions (of ΔU) constant during the current increment, the strain increment is calculated by the ABAQUS FE code as $\Delta\epsilon = \ln \Delta V$ (and then projected onto the local frame).

The trial stress Σ^{tr} is defined as the stress that would be obtained if $\Delta\epsilon$ were a purely elastic deformation

$$\Sigma^{tr} := \Sigma_n + C : \Delta\epsilon \tag{B.1}$$

Clearly, if $f(\Sigma^{tr}) - H(\bar{\epsilon}_n^p) \leq 0$ the current increment $\Delta\epsilon$ is indeed elastic and the update is simply

$$\Sigma_{n+1} = \Sigma^{tr}, \quad \bar{\epsilon}_{n+1}^p = \bar{\epsilon}_n^p, \quad E^p = C \tag{B.2}$$

If $f(\Sigma^{tr}) - H(\bar{\epsilon}_n^p) > 0$, then $\Delta\epsilon$ cannot be entirely elastic (for otherwise $\bar{\epsilon}_{n+1}^p = \bar{\epsilon}_n^p$, a contradiction) and hence the following inequality must hold

$$\Delta\bar{\epsilon}^p := \int_{t_n}^{t_{n+1}} \dot{\bar{\epsilon}}^p dt = \bar{\epsilon}_{n+1}^p - \bar{\epsilon}_n^p > 0 \tag{B.3}$$

The constitutive system (13)–(17) has to be integrated such that at the end of the time step the yielding condition and the flow (normality) rule are both satisfied. The numerical integration scheme must then necessarily be implicit (e.g. backward Euler: evaluations at the end of the time step). Integrating eq. (17) leads to

$$\begin{aligned}\Sigma_{n+1} - \Sigma_n &= \int_{t_n}^{t_{n+1}} \dot{\Sigma} dt \approx C : \left[\Delta\epsilon - \frac{\partial f}{\partial \Sigma}(\Sigma_{n+1}) \int_{t_n}^{t_{n+1}} \dot{\bar{\epsilon}}^p dt\right] \\ &= C : \left[\Delta\epsilon - \frac{\partial f}{\partial \Sigma}(\Sigma_{n+1})\Delta\bar{\epsilon}^p\right]\end{aligned} \tag{B.4}$$

and the system of equations to be solved for the new stress state and the increment (B.3) is $F(x) = 0$, where

$$F(x) = \begin{bmatrix} F_1(x) \\ F_2(x) \end{bmatrix} = \begin{bmatrix} S : \Delta\Sigma + \Delta\bar{\epsilon}^p \dfrac{\partial f}{\partial \Sigma}(\Sigma_{n+1}) - \Delta\epsilon \\ f(\Sigma_{n+1}) - H(\bar{\epsilon}_n^p + \Delta\bar{\epsilon}^p) \end{bmatrix}, \text{ with } x := \begin{bmatrix} \Delta\Sigma^p \\ \Delta\bar{\epsilon} \end{bmatrix} \tag{B.5}$$

with $S := C^{-1}$ denoting the compliance tensor and $\Delta\Sigma := \Sigma_{n+1} - \Sigma_n$. This system is solved with the Newton–Raphson algorithm:

$$\begin{aligned} &x_{k+1} = x_k + \delta x, \text{ where } \frac{\partial F}{\partial x}(x_k)[\delta x] = -F(x_k), \text{ and} \\ &\delta x := \begin{bmatrix} \delta\Delta\Sigma^p \\ \delta\Delta\bar{\epsilon} \end{bmatrix} \end{aligned} \tag{B.6}$$

The starter point for the sequence of Newton–Raphson iterations is $x_0 = (\Sigma^{tr} - \Sigma_n, 0)$. Denoting with $\Delta\Sigma_{(k)}$, $\Sigma_{(k)} = \Sigma_n + \Delta\Sigma_{(k)}$, and $\Delta\bar{\epsilon}_{(k)}^p$ the k-th iterations of $\Delta\Sigma$, Σ_{n+1}, and $\Delta\bar{\epsilon}^p$, respectively, and further

$$M(x) := S + \Delta\bar{\epsilon}^p \frac{\partial^2 f}{\partial\Sigma\partial\Sigma}(\Sigma), \quad \bar{\epsilon}_{(k)}^p := \bar{\epsilon}_n^p + \Delta\bar{\epsilon}_{(k)}^p \tag{B.7}$$

the linear system for increments reads

$$\begin{cases} M(x_k) : \delta\Delta\Sigma + \dfrac{\partial f}{\partial \Sigma}(\Sigma_k)\delta\Delta\bar{\epsilon}^p = -F_1(x_k) \\ \dfrac{\partial f}{\partial \Sigma}(\Sigma_k) \cdot \delta\Delta\Sigma - H'\left(\bar{\epsilon}_k^p\right)\delta\Delta\bar{\epsilon}^p = -F_2(x_k). \end{cases} \tag{B.8}$$

Solving the second equation above for $\delta\Delta\bar{\epsilon}^p$,

$$\delta\Delta\bar{\epsilon}^p = \frac{1}{H'\left(\bar{\epsilon}_k^p\right)}\left[F_2(x_k) + \frac{\partial f}{\partial \Sigma}(\Sigma_k) \cdot \delta\Delta\Sigma\right] \tag{B.9}$$

and substituting in the first equation leads to the following linear system

$$\begin{aligned} &\left[H'\left(\bar{\epsilon}_{(k)}^p\right) M(x_k) + \frac{\partial f}{\partial \Sigma}\left(\Sigma_{(k)}\right) \otimes \frac{\partial f}{\partial \Sigma}\left(\Sigma_{(k)}\right)\right] : \delta\Delta\Sigma \\ &= -\left[H'\left(\bar{\epsilon}_{(k)}^p\right) F_1(x_k) + F_2(x_k)\frac{\partial f}{\partial \Sigma}\left(\Sigma_{(k)}\right)\right] \end{aligned} \tag{B.10}$$

that can be efficiently solved for the increment $\delta\Delta\Sigma$ by using the Cholesky decomposition of the positive definite matrix on the left hand side of the above equation. Then $\delta\Delta\bar{\epsilon}^p$ is calculated with eq. (B.9). The stress and hardening parameter increments are then updated by the Newton–Raphson formula (B.6) and if the norm of the residual has decreased under a desired tolerance, that is, if $|F(x_{k+1})| = \sqrt{[F_1(x_{k+1})]^2 + [F_2(x_{k+1})]^2} \leq T$, then the iteration sequence stops and the last Newton–Raphson update is accepted as solution. Usually a tolerance of $T \approx 10^{-7}$ is sufficient and is achieved within $k \approx 6$ iterations. Since the Newton–Raphson sequence is known to converge slowly if the initial estimate is not close to the solution, an additional precaution was taken in the present implementation by using a quadratic approximation of $|F|$ along the Newton–Raphson direction to perform a line search in this direction. This ensures that $|F|$ is indeed decreasing during each Newton–Raphson step.

Finally, by following the well known derivation, e.g. Simo and Hughes (1998), from the consistency condition $\dot{f}(\Sigma) = 0$, holding true during continuous plastic flow, the algorithmic tangent modulus is estimated as

$$E^p = M - \frac{1}{\dfrac{\partial f}{\partial \Sigma} \cdot \left(M : \dfrac{\partial f}{\partial \Sigma}\right) + H'} \left(M : \frac{\partial f}{\partial \Sigma}\right) \otimes \left(M : \frac{\partial f}{\partial \Sigma}\right) \tag{B.11}$$

Appendix C. Yield surface models and deep drawing parameters

The parameters listed next define plane stress restrictions of Yld2004B. Only for AA2090-T3 a 3D analysis was conducted with Model 0. For this model the additional parameters were as follow: $\alpha_8^{(1)} = 1.024$, $\alpha_9^{(1)} = 1.069$, $\alpha_8^{(2)} = 1.052$, $\alpha_9^{(2)} = 1.147$, (data from Barlat et al. (2005)). Each deep drawing simulation was performed in three (ABAQUS) Steps, ABAQUS (2004). In Step 1 the holder (initially positioned at a small distance above the blank) was moved just enough to make contact with the blank. In Step 2, the holding force (a quarter of the value reported in Table C4) was applied on holder (replacing the previous boundary condition in the z-direction on the holder). The blank holding force is small,

Table C1
Yld2004B parameters of the image stresses (I.S.) for the three models of AA2090-T3.

Model	I. S.	α_1	α_2	α_3	α_4	α_5	α_6	α_7
Model 0	$\Sigma^{(1)}$	0.2888	0.3587	0.2816	0.3607	0.1046	−0.7339	0.9543
	$\Sigma^{(2)}$	0.4860	−0.4952	−0.0946	0.4807	−0.7898	0.4345	1.4046
Model 1	$\Sigma^{(1)}$	0.6512	0.8920	0.5346	1.2609	0.2362	0.7385	1.2273
	$\Sigma^{(2)}$	0.5578	0.6209	0.5570	0.6171	0.7442	0.0490	1.1413
	$\Sigma^{(3)}$	−0.8129	0.0827	−1.1632	0.0834	−0.8808	1.1761	1.0930
Model 2	$\Sigma^{(1)}$	0.6402	1.1004	0.6412	1.0965	0.0453	0.3598	1.2750
	$\Sigma^{(2)}$	0.6344	0.6472	0.6343	0.6479	0.7549	0.0625	1.1040
	$\Sigma^{(3)}$	−0.9666	0.1918	−1.1524	0.1313	−0.7071	1.2418	0.9613

Table C2
Yld2004B parameters of the image stresses (I.S.) for the two models of AA3104-H19.

Model	I. S.	α_1	α_2	α_3	α_4	α_5	α_6	α_7
Model 1	$\Sigma^{(1)}$	0.0625	0.7591	−0.2232	0.9667	0.3701	−0.3824	0.6003
	$\Sigma^{(2)}$	0.1946	0.6133	−0.1964	0.2633	0.7090	−0.0710	1.0652
	$\Sigma^{(3)}$	0.8223	0.2815	−1.1554	0.2047	−0.0704	−0.6983	1.7212
Model 2	$\Sigma^{(1)}$	−0.0342	0.8289	−0.1271	0.9418	0.3275	−0.3545	0.5814
	$\Sigma^{(2)}$	0.3071	0.5683	−0.2466	0.3719	0.6747	−0.1014	1.0936
	$\Sigma^{(3)}$	0.9689	0.1570	−1.1462	0.3571	0.0024	−0.7533	1.7243

Table C3
Parameters of the image stresses (I.S.) for the Yld2004B model of RMAT.

Model	I. S.	α_1	α_2	α_3	α_4	α_5	α_6	α_7
RMAT	$\Sigma^{(1)}$	0.85633	0.19762	−0.36142	0.83550	0.16410	0.83525	1.92838
	$\Sigma^{(2)}$	0.33129	0.42931	−0.13865	0.44233	0.25497	−0.26778	−0.00499
	$\Sigma^{(3)}$	1.04024	−0.20040	0.78756	−1.13917	−1.05776	0.87730	−1.09652

just to prevent wrinkling (out of plane local bending) of the sheet during drawing. Finally, in Step 3, the drawing step, the punch is moved vertically, hence drawing the blank into the die cavity. Large increments in this step were not allowed, to ensure the best conditions for the kinematic assumptions of the FE code, and to avoid large variations in the input to the constitutive subroutine: the maximum time increment in Step 3 was set to 0.001. The contact in the 3D simulation was "hard" (with the nonstick condition), while the 2D simulations used the soft contact, with exponential contact-closure distance. The contact pressure was approximated as $p \approx F/\{\pi[R_b^2 - (R_d + r_d)^2]\}$, while the zero contact distance was set to 0.001. The tools were modeled as analytical rigid. To prevent convergence problems during the last moments of the drawing phase, an elastic (stiff) ring was placed beneath the die at a distance of 0.005 mm for 2D simulations and 0.1 mm for the 3D simulation. With soft contact between holder and ring in Step 3, the ring stops the holder when the blank leaves the flange area.

Table C4
Deep drawing parameters (dimensions in millimeters).

Material	R_b	thickness	R_p	r_p	R_d	r_d	F holder	Friction
AA2090-T3	79.38	1.6	48.73	12.70	50.74	12.70	22.2 kN	0.1
AA3104-H19	30.0	0.241	16.5	5.0	16.82	2.5	6.9 kN	0.025

Finally, the hardening of AA2090-T3 and RMAT was described as $H(\bar{\epsilon}^p) = A(B + \bar{\epsilon}^p)^C$, with $A = 646.0$ MPa, $B = 0.025$, $C = 0.227$, data from Yoon et al. (2006), while that of AA3104-H19 as $H(\bar{\epsilon}^p) = A + (B + C\bar{\epsilon}^p)[1 - \exp(-D\bar{\epsilon}^p)]$, with $A = 276.0$ MPa, $B = 43.6$ MPa, $C = 116.2$ MPa, $D = 50.76$, data from Aretz et al. (2010).

References

ABAQUS 6.5, 2004. Reference Manuals. Hibbit, Karlsson and Sorensen, Pawtucket, RI.

Aretz, H., Aegerter, J., Engler, O., 2010. Analysis of Earing in Deep Drawn Cups. Numiform-2010 Proceedings.

Arminjon, M., Bacroix, B., Imbault, D., Raphanel, J.L., 1994. A fourth order plastic potential for anisotropic metals and its analytical calculation from texture function. Acta Mech. 107, 33–51.

Atluri, S., 1984. On constitutive relations at finite strain: hypo-elasticity and elasto-plasticity with isotropic or kinematic hardening. Comput. Methods Appl. Mech. Eng. 43, 137–171.

Barlat, F., Aretz, H., Yoon, J.W., Karabin, M.E., Brem, J.C., Dick, R.E., 2005. Linear transformation based anisotropic yield function. Int. J. Plast. 21, 1009–1039.

Belytschko, T., Liu, W.K., Moran, B., 2000. Nonlinear Finite Elements for Continua and Structures. John Wiley & Sons, Chichester, England.

Boehler, J.P., 1987. Application of Tensors Functions in Solids Mechanics, CISM Courses and Lectures, vol. 292. Springer, Berlin.

Duchene, L., 2003. FEM study of metal sheets with a texture based, local description of the yield locus, PhD Dissertation, Univ. de Liege.

Hershey, A.V., 1954. The plasticity of an isotropic aggregate of anisotropic face centred cubic crystals. J. Appl. Mech. 21, 241–249.

Hill, R., 1950. The Mathematical Theory of Plasticity. Clarendon Press, Oxford.

Hill, R., 1990. Constitutive modeling of orthotropic plasticity in sheet metals. J. Mech. Phys. Solids 38, 405–417.

Hosford, W.F., 1972. A generalized isotropic yield criterion. J. Appl. Mech. 39, 607–609.

Hosford, W.F., 1993. The Mechanics of Crystals and Textured Polycrystals. Oxford University Press, New York.

Hosford, W.F., Caddell, R.M., 1993. Metal Forming: Mechanics and Metallurgy, second ed. Prentice Hall, Upper Saddle River.

Karafillis, A.P., Boyce, M.C., 1993. A general anisotropic yield criterion using bounds and a transformation weighting tensor. J. Mech. Phys. Solids 41, 1859–1886.

Kim, J.H., Lee, M.G., Barlat, F., Wagoner, R.H., Chung, K., 2008. An elasto-plastic constitutive model with plastic strain rate potentials for anisotropic cubic metals. Int. J. Plast. 24, 2298–2334.

Kocks, U.F., Tome, C.N., Wenk, H.R., 2000. Texture and Anisotropy. Cambridge University Press.

Nelder, J.A., Mead, R., 1965. A simplex method for function minimization. Comp. J. 7, 308–313.

Rabahallah, M., Balan, T., Bouvier, S., Teodosiu, C., 2009. Time integration scheme for elastoplastic models based on anisotropic strain-rate potentials. Int. J. Numer. Methods Eng. 80, 381–402.

Simo, J., Hughes, T.J.R., 1998. Computational Inelasticity. Springer-Verlag, New York.

Soare, S., Yoon, J.W., Cazacu, O., 2008. On the use of homogeneous polynomials to develop anisotropic yield functions with applications to sheet forming. Int. J. Plast. 24, 915–944.

Soare, S., Barlat, F., 2010. Convex polynomial yield functions. J. Mech. Phys. Solids 58, 1804–1818.

Tugcu, P., Neale, K.W., 1999. On the implementation of anisotropic yield functions into finite strain problems of sheet metal forming. Int. J. Plast. 15, 1021–1040.

Van Houtte, P., Clarke, A.P., Saimoto, S., 1993. In: Morris, J.G., Westerman, E.J., Morris, P.L. (Eds.), Aluminum Alloys for Packaging. TMS, Warrendale, PA, pp. 261–273.

Van Houtte, P., Kanjarla, A.K., Van Bael, A., Seefeldt, M., Delannay, L., 2006. Multi-scale modeling of the plastic anisotropy and deformation texture of poly-crystalline materials. Eur. J. Mech. A Solids 25, 634–648.

Yoon, J.W., Barlat, F., Chung, K., Pourboghrat, F., Yang, D.Y., 1998. Earing predictions based on asymmetric nonquadratic yield function. Int. J. Plast. 16, 1075–1104.

Yoon, J.W., Barlat, F., Dick, R.E., Karabin, M.E., 2006. Prediction of six or eight ears in a drawn cup based on a new anisotropic yield function. Int. J. Plast. 22, 174–193.